

N O T I C E

THIS DOCUMENT HAS BEEN REPRODUCED FROM
MICROFICHE. ALTHOUGH IT IS RECOGNIZED THAT
CERTAIN PORTIONS ARE ILLEGIBLE, IT IS BEING RELEASED
IN THE INTEREST OF MAKING AVAILABLE AS MUCH
INFORMATION AS POSSIBLE

INSTABILITY OF A SUPERSONIC SHOCK FREE ELLIPTIC JET¹

Roy S. Baty²

Sandia National Laboratories, Albuquerque, NM 87185

SAND--90-0179C

John M. Seiner³

DE91 001231

and

Michael K. Ponton⁴

NASA Langley Research Center, Hampton, VA 23665

ABSTRACT

This paper presents a comparison of the measured and the computed spatial stability properties of an aspect ratio 2 supersonic shock free elliptic jet. The shock free nature of the elliptic jet provides an ideal test of the validity of modeling the large scale coherent structures in the initial mixing region of non-circular supersonic jets with linear hydrodynamic stability theory. Both aerodynamic and acoustic data were measured. The data are used to compute the mean velocity profiles and to provide a description of the spatial composition of pressure waves in the elliptic jet. A hybrid numerical scheme is applied to solve the Rayleigh problem governing the inviscid linear spatial stability of the jet. The measured mean velocity profiles are used to provide a qualitative model for the cross sectional geometry and the smooth velocity profiles used in the stability analysis. Computational results are presented for several modes of instability at two jet cross sections. The acoustic measurements show that a varicose instability is the jet's preferred mode of motion. The stability analysis predicts that the Strouhal number varies linearly as a function of axial distance in the jet's initial mixing region, which is in good qualitative agreement with previous measurements.

1.0 INTRODUCTION

For years the origin of noise production by supersonic round jets has been pursued vigorously both theoretically and experimentally. Several theoretical models exist to predict this noise, but the most successful concept to date is the quasi-linear instability wave model. Tam, ref. 1, has applied this model to provide a comprehensive prediction for both jet and shock noise components. A natural extension of this model is its application to non-circular super-

sonic jets. Morris, ref. 2, applied the instability wave model to elliptic jets and was able to determine that as the exit plane momentum thickness increases, the dominant spatial mode of instability occurs along the major axis. While this work provided a foundation for analysis of non-circular jets, only those velocity profiles that allowed a separable solution were applicable. Thus the analysis could not be performed for those flows whose jet column deformed as it evolved downstream. To overcome this important limitation, Baty and Morris, ref. 3, introduced a scheme to compute non-separable solutions of the stability equation which occur when the mean velocity profile is deformed as the flow evolves downstream. This method is based on a conformal mapping of the irregularly shaped jet cross section along with a hybrid numerical scheme.

In the present paper the hybrid numerical scheme is applied to solve the Rayleigh equation which governs the inviscid linear spatial stability of an elliptic jet with an initial aspect ratio of 2. An elliptic nozzle was designed for this study to produce a shock free flow of Mach 1.5. The spatial modes of instability and neutral instability frequencies as a function of axial location were calculated. An experimental program was also conducted to determine the preferred spatial mode of instability and identify the Strouhal number associated with peak amplitude noise radiation from the jet. Previous studies have shown that the frequency for the most unstable shear layer mode is directly related to this Strouhal number. Mean axial velocity profiles and contours were also obtained to improve the numerical model. Only data associated with the operation of the supersonic nozzle at its shock free design point are presented in this paper.

2.0 EXPERIMENTAL FACILITIES

The elliptic nozzle tested was designed to produce Mach 1.5 axial flow at the exit. The internal geometry is presented in figure 1. The convergence section consisted of a circular to elliptic transition leading to an elliptic subsonic contraction of aspect ratio 2. This

¹This work was done under NASA Research Center Grant NAG-1-857 entitled, "Reynolds Stress Closure in Jet Flows Using Wave Models."

²Senior Member of Technical Staff, Member AIAA.

³Senior Research Scientist, Associate Fellow AIAA.

⁴Research Engineer, Member AIAA.

aspect ratio was held constant throughout the nozzle divergence section to the exit where the dimensions are 2.000 by 1.000 inches. The axial length of the divergence section is 5.015 inches.

A nozzle design method developed by Seiner, et al., ref. 4, using both one and two dimensional inviscid isentropic theory, was applied to generate the interior wall coordinates. The design goal was to produce uniform Mach 1.5 parallel flow at the nozzle exit where the pressure waves in the plume differed from the ambient pressure by less than 10 percent. Shock waves that satisfy this pressure minimization criterion produce insignificant levels of shock noise relative to other jet noise sources. Since the nozzle design procedure is inviscid, the nozzle was operated at a nozzle pressure ratio of NPR = 3.78 to account for boundary layer effects. At this NPR the flow only contained weak waves with an exit Mach number of 1.52.

Aerodynamic measurements were performed in the NASA Langley Jet Noise Laboratory. These measurements utilized total and static pressure probes designed for supersonic flow. The total pressure probe consisted of a 0.060 inch diameter tube with a 0.020 inch sensor port where the probe inlet was machined flat to create a well defined detached shock when submerged in supersonic flow. The static pressure probe, based on the design of Pinckney ref. 5, was a dual conical type which recovers the tip static pressure faster than conventional static probes. This allows the holes to be positioned near the probe tip which is important for flows with large axial pressure gradients. Both probes were installed in a probe wing designed for supersonic flow which was attached to a remote controlled three dimensional traversing mechanism capable of 0.001 inch movements. Centerline data were collected as well as one dimensional pressure profiles and two dimensional pressure maps at various axial positions in the jet.

A schlieren system was assembled in the Jet Noise Lab to give an indication of the density gradient field in the flow. A vertical knife edge was used to give the effect of the density gradient component in the direction of the flow. Figures 2a and 2b show the schlieren optical records in planes parallel to the major and minor axes respectively, ref. 4. Waves associated with the weak variations in axial static pressure can be seen in the figures due to the high sensitivity of the schlieren apparatus.

Also collected in this facility were near-field acoustic measurements using an elliptic microphone array, figure 3. The array consisted on twelve Bruel and Kjaer 1/4 inch pressure microphones positioned to form an aspect ratio 2 ellipse whose major axis length was 5.0 inches. The positions of the microphones in

Cartesian coordinates (origin at the jet axis) are given in parenthesis in figure 3 for a single quadrant. The microphones were positioned perpendicular to the jet axis in the nozzle exit plane and spaced at equal elliptic arc lengths of 1.009 inches on the array. The data were gathered using a wide band analog magnetic tape recorder band limited to 20 kHz. Spectra were acquired in real time via a Scientific Atlanta Model SD380 Fast Fourier Transform (FFT) analyzer. By heating the flow electrically, all measurements were obtained at a stagnation temperature of 40 degrees Celsius.

Additional acoustic data were collected in the NASA Langley Anechoic Noise Facility, ref. 6. Twenty six Bruel and Kjaer 1/4 inch microphones were positioned on a linear array parallel to the jet axis and perpendicular to the nozzle's minor axis, i.e., facing the nozzle exit's wide dimension. Figure 4 shows the seven radial positions used for the array, where D_{eq} is the elliptic nozzle's equivalent diameter relative to a round nozzle defined by:

$$D_{eq} = 2B\sqrt{AR} \quad (2.1)$$

where B is the nozzle minor radius and AR is the nozzle aspect ratio. In the present case D_{eq} is equal to 1.414 inches. The microphones were spaced at equal intervals of 3 equivalent diameters. The fourteenth microphone from the top of the array was located in the nozzle exit plane. The acoustic signals were tape recorded using intermediate band recorders limited to 20 kHz and were post-test processed using the SD380 FFT analyzer. Because no electric heat was available in this facility, the stagnation temperature varied from approximately 26 to 31 degrees Celsius throughout the experiment.

3.0 EXPERIMENTAL RESULTS

This section presents both near field acoustic and plume mean flow data. Even though measurements were obtained for a wide range of nozzle pressure ratios, only the fully expanded results are presented here. The linear inviscid Rayleigh equation, as used in the present analysis, is not valid for plumes that contain shocks. Thus all data presented was obtained by operating the elliptic nozzle at a nozzle pressure ratio of 3.76, which corresponds to a fully expanded Mach number of 1.52.

3.1 Acoustic Measurements

As described in section 2.0, near field acoustic data was obtained using a 26 element linear microphone array and a 12 microphone element array with sensors positioned along an elliptic curve. The linear array provided data that enabled determination of impor-

tant spectral and directional characteristics of the radiated sound field. The 12 element array, which had sensors distributed equidistant along an ellipse surrounding the nozzle enabled determination of the jet's preferred spatial structure.

The linear array was positioned at seven radial locations from the minor axis, thus providing a total of 182 measured points. The radial locations varied from 10 to 40 D_{eq} in 5 D_{eq} increments. Figure 5 shows contours of equal overall sound pressure level (OASPL) obtained by applying the DI-3000 contour routine to the measured data test matrix. The scaled position of the nozzle is also shown in the figure. The contours are presented in 2 dB increments and range from a value of 104 dB to 132 dB.

The contour data of figure 5 clearly shows that most noise emitted from the elliptic nozzle's plume is directed at a narrow angle to the direction of the flow. The majority of noise is contained within a 40 degree cone centered at the nozzle exit. This noise is of prime importance to the analysis contained in this paper. The data suggests that this noise originates from a region between 5 and 6 diameters from the nozzle exit and is directed at 30 degrees to the jet axis. The contour data shows no evidence of screech or broadband shock associated noise, thus indicating that the nozzle design procedure, ref. 4, was successful. The contour data results are also consistent with those measured by Yu and Dosanjh, ref. 7, for the fully expanded Mach 1.5 axisymmetric nozzle and those predicted by Tam and Burton, ref. 8. One significant difference between the round and elliptic jets is that acoustic radiation from the elliptic jet has an apparent origin closer to the nozzle exit than is found for the round jet. Based on velocity measurements shown in the next section, the convection velocity of the large scale turbulent structures in the jet shear layer is subsonic. Thus the sound radiation would not include noise due to the eddy Mach wave mechanism.

A typical narrow band spectrum of the noise radiated into the cone is given in figure 6. The location of the microphone for this spectrum is shown in figure 5 as the solid circle in the upper left-hand quadrant of the contour. The frequency corresponding to the spectrum peak amplitude is labelled as f_c in figure 6. Since the spectrum peak is broad, the value $f_c = 2.4$ kHz only represents a nominal value. Based on this frequency, however, the nondimensional Strouhal number,

$$St_c = \frac{f_c D_{eq}}{V} = 0.19 \quad (3.1)$$

compares well with the value $St_c = 0.22$ previously reported by Seiner, ref. 9, for the Mach 1.5 axisymmetric jet.

3.2 Measured Modes of Instability

An example nozzle exit microphone spectrum is shown in figure 7. This spectrum is from the microphone located along the minor axis in the direction of the linear array microphones. Even though the spectrum appears irregular with multiple broadband spectrum peaks, the Strouhal number $St_c = 0.19$ component, identified in figure 6, is clearly present. This suggests that the major noise component may also emit energy directed upstream from the region between 5 and 6 D_{eq} .

The nozzle exit array data was used to evaluate the preferred spatial structure of the large scale instabilities in the jet plume. This was accomplished by Fourier decomposition of the azimuthal variation of the measured cross correlation coefficients between the 12 array microphones for several octave bands of noise. Figures 8a, 8b, and 8c show the results of this analysis for the Strouhal number bands $St_c = 0.08, 0.13,$ and 0.16 . The cross correlation coefficient amplitudes are presented in terms of the normalized arc distance around the array. The arc distance is the fundamental period for the Fourier decomposition, each microphone being spaced in equal increments of arc length. Microphone 4, which lies along the minor axis is used as the reference microphone in computing the cross correlation coefficient. Each figure contains summary findings of the modal content associated with each octave band of noise. Here A_0 denotes the varicose or axisymmetric mode. The amplitudes associated with even symmetry are given by A_n , and those with odd symmetry by B_n . Thus an equal combination of A_1 and B_1 modal amplitudes will produce a flapping motion in the jet column.

The modal decomposition presented in figures 8 indicates that only the varicose and flapping modes have sufficient amplitudes to be of interest. All higher order modes are insignificant. The varicose instability surfaces as the dominant mode for all three octave bands. The predominance of the varicose mode increases with increasing Strouhal number, as shown by comparing figures 8a, 8b, and 8c. Thus for the principle noise producing mechanism, the dominant mode of instability is the varicose mode.

An important point should be made concerning Fourier decomposition of the array element cross correlation coefficients. The Fourier modal amplitudes depend on the coordinate surface on which the microphones are located. In the present analysis, microphones are located around the elliptic nozzle along an elliptic cylindrical coordinate, (ECC). For round jets microphones are generally distributed along a circular path. The choice of microphone orientation is dictated by a predetermined understanding of the nature

of the noise generation process. For round jets we expect the noise source mechanism to be axisymmetric. For elliptic jets this type of thinking can be primitive. If the jet column remains undistorted, that is, it has a spread rate that does not depend on azimuth, then the ECC may represent a prudent choice. If however, significant distortion of the jet column takes place, then another coordinate system needs to be found for synthesizing the fundamental modes. Since only two modes were found to contain significant energy, the present analysis implies that the choice of the present coordinate system may have been correct. In the following section the flow measurements will also show, at least to the end of the potential core, the jet column undergoes only minor distortion.

3.3 Flow Field Measurements

As discussed above, application of the linear inviscid instability wave model requires empirical input of the mean velocity distribution throughout the jet. Toward this end, the mean axial velocity was measured. Both the minor and major axis surveys were made at seven axial locations ranging from 0.2 to 10.0 D_{eq} . In addition, a high resolution traverse of the centerline distribution of axial velocity was made from the nozzle exit to 28 D_{eq} along with four 351 point quadrant flow maps at the 0.25, 0.50, 0.75, and 1.00 potential core lengths.

The centerline velocity distribution is measured to determine the length of the jet's potential core and for supersonic jets to gage the adequacy of the nozzle design method to achieve shock free flow. Figure 9 shows the measured centerline velocity when operating the elliptic nozzle at its design point. The axial variations in mean flow velocity in the first 7 D_{eq} are due to imperfections in the nozzle design. These variations are often stronger with round jets, due to their focusing of waves along the jet centerline. Based on this data it is possible to determine the axial extent of the potential core, L_c , as that point where the mean velocity is 99 percent of the jet exit velocity. This point occurs at $X_c = 5.06 D_{eq}$ as is more clearly shown in the expanded view of figure 10.

Figures 11a and 11b show, respectively, 351 point axial mean flow maps for $X = 0.25L_c$ and $0.50L_c$. The contours range from a value of 100 to 1400 ft/sec in 100 ft/sec increments. In general the flow appears to distort gradually.

The initial distribution of momentum thickness has been used in the past, for example by Ho and Gutmark, ref. 10, and by Bridges and Hussain, ref. 11, as a length scale for the initial turbulent shear layer. The azimuthal distribution of the momentum thickness around the periphery of the nozzle exit controls

the initial role-up of shed vorticity, and the eventual distortion of the jet column. The axial distribution of the momentum thickness along both the major and minor axis then would provide an indication of distortion of the jet column with downstream distance. For compressible flows the momentum thickness is defined by

$$\theta = \int_0^{\infty} \frac{\rho V}{(\rho V)_0} \left(1 - \frac{V}{V_0}\right) dr \quad (3.2)$$

where V_0 is the value of centerline velocity at a given axial location.

The mean velocity profiles along the major and minor axis were integrated numerically for momentum thickness at the seven axial stations. Figure 12 shows the resulting axial momentum thickness for both major and minor axes. As can be observed, the momentum thickness is nearly equal on both major and minor axes over the length of the potential core. This suggests that the initial strength of shed vorticity is constant around the periphery of the nozzle, thus producing little tendency for distortion of the jet column as the flow evolves. In the potential core region the momentum thickness also grows linearly, a result consistent with the well known behavior of round jets. Near the end of the potential core the momentum thickness along the major axis grows at a much greater rate than that along the minor axis. Based on figure 12, this occurs just before the end of the potential core.

4.0 NUMERICAL MODEL

Consider the shock free jet issuing from the aspect ratio 2 elliptic nozzle described in section 2.0, with a uniform exit Mach number of 1.52. To establish the governing stability equation, assume a Cartesian coordinate system with the jet axis aligned in the z direction. Let $W(x, y)$ denote the mean axial velocity of the jet. The local parallel flow assumption of hydrodynamic stability is applied neglecting the mean velocity components in the x and the y directions. If this assumption is not made and the effects of flow divergence are considered, a problem results which requires a multiple-scale analysis. Such effects are not addressed in the present study.

A linear, elliptic, partial differential equation for the pressure associated with the large scale coherent structures is obtained by taking the divergence of the momentum equation and using the ideal gas law with the equations of continuity and energy. The resulting equation is linearized about the mean flow. The velocity fluctuations are eliminated in favor of the pressure fluctuation using the linearized momentum equations. Then assuming that the pressure fluctuation may be

written in the form:

$$p(x, y, z, t) = \hat{p}(x, y) \exp i\gamma \quad (4.1)$$

where

$$\gamma = \alpha z - \omega t \quad (4.2)$$

α is the axial wave number, and ω is the instability wave frequency, the equation for \hat{p} may be expressed as:

$$(\Delta - \alpha_c^2)\hat{p} + \frac{2\alpha}{(\omega - \alpha W)} \nabla \hat{p} \cdot \nabla W = 0 \quad (4.3)$$

Equation (4.3) is the Rayleigh equation governing the inviscid, compressible, isothermal spatial stability of the elliptic jet. In (4.3), the compressible wavenumber, α_c , is defined as:

$$\alpha_c^2 = \alpha^2 - M_j^2(\omega - \alpha W)^2 \quad (4.4)$$

where M_j is the exit Mach number of the jet, which is 1.52 in the present study. The equations exhibited have been non-dimensionalised with respect to the pressure, temperature, and velocity at the jet exit. The length scale is based on an equivalent radius defined by:

$$L = \sqrt{AB} = D_{eq}/2 \quad (4.5)$$

where A and B are the major and minor dimensions of the jet, respectively. In order to determine the pressure \hat{p} , in equation (4.3), boundary conditions must be added. In this case \hat{p} satisfies:

$$\hat{p} \rightarrow 0 \quad \text{as} \quad |x| \rightarrow +\infty \quad (4.6)$$

and

$$\hat{p} \text{ is finite as } |x| \rightarrow 0 \quad (4.7)$$

The computational goal in solving the stability problem defined by equations (4.3) to (4.6) is to determine the complex wavenumber spectrum, α_c , for a given frequency, ω .

4.1 Jet Model

To analyse the elliptic jet it is advantageous to introduce a new coordinate system. Transformations are used to map standard computational rectangles onto regions modeling the elliptic jet's shear layer cross sections. Conformal maps are applied to generate the necessary transformations. These maps are desirable analytically, since they generate diagonal metric terms which simplify the computational form of the Rayleigh equation.

Conformal maps may be constructed very efficiently for a wide range of simply and doubly connected regions bounded by elliptic curves, Baty, ref. 12. In the

present study, the conformal maps will be defined by the complex cosine:

$$w = a \cos z \quad \text{for} \quad z = y^1 + iy^2 \quad (4.8)$$

where a is a real number. Here equation (4.8) is equivalent to introducing an elliptic cylindrical coordinate system. In this coordinate system, the Rayleigh equation becomes:

$$(\Delta - \hat{g}\alpha_c^2)\hat{p} + \frac{2\alpha}{(\omega - \alpha W)} \nabla \hat{p} \cdot \nabla W = 0 \quad (4.9)$$

where metric term \hat{g} is defined by:

$$\hat{g} = |a \sin z|^2 \quad (4.10)$$

The ECC generate confocal elliptic regions which capture the qualitative shape of the elliptic jet's cross section. The simple conformal maps defined by (4.8) were applied to model the jet's shear layer geometry rather than the more realistic models developed in ref. 12 for two reasons. Firstly, the use of confocal coordinate allowed the results of the numerical scheme to be validated for an incompressible case given in Morris, ref. 2. Secondly, a coordinate system was needed which modeled the gross physical characteristics of the elliptic jet's cross sectional geometry. Using the ECC the half velocity curve in the shear layer is approximated closely. Figure 13 shows a typical jet cross section and the half velocity curve in nondimensional coordinates.

Furthermore, it is not clear that using a different conformal map would yield a more accurate shear layer model. The measured jet velocity contours of figures 11 indicate that the nozzle has a slight imperfection along the wall joint on the minor axis near the exit plane. This imperfection was caused by a mismatch of the nozzle halves. The measured velocity profiles show that the nozzle distorts the elliptic jet by forcing the jet to bulge out on the top half of the jet. This phenomenon is shown in figure 11a. The existing conformal mapping techniques, ref. 12, developed to model arbitrary elliptic jets, are unable to generate the coordinate transformations needed to analyse such small scale flow imperfections. Therefore, the most simple coordinate transformations which capture the global features of the jet's cross sections were introduced into the numerical model.

The mean velocity profile used in the computation is based on a generalization of the profile given by Michalke, ref. 13. Details of the development of the velocity profile in ECC can be found in Morris, ref. 14. For all the computations the mean axial velocity profile is assumed to be given by:

$$W(y^2) = \frac{1}{2}(1 + \tanh(g(y^2))) \quad (4.11)$$

where

$$g(y^2) = \frac{B}{2\theta_B} \left(1 - \frac{a \cos(y^1 + iy^2)}{a \cos(y^1 + iy_0^2)}\right) \quad (4.12)$$

$$\text{for } y_0^2 \leq y^2 < \infty \quad (4.13)$$

In equations 4.11 to 4.13, y_0^2 is the half velocity point, B is the length of the minor axis θ_B is the momentum thickness on the minor axis and y_0^2 is a real value satisfying:

$$\tanh(g(y_0^2)) \approx 1 \quad (4.14)$$

For the subsonic low Reynolds number jet, Ho and Gumark, ref. 15, found very good agreement between the profile defined by equations 4.11 to 4.14 and experiment. Comparing figures 11a and 13 shows that the velocity profile describes qualitatively the velocity curves in the physical jet cross section.

For the present supersonic elliptic jet, the off axis mean velocity measurements, figure 11a, suggest that the mean velocity may be approximated accurately using a function which depends on one coordinate direction. While the experimental data was not used to generate the mean velocity profiles needed by the computations, it was used to approximate the cross sectional geometry of the jet. It is believed that data without the minor axis distortion should be used to approximate smoothly the mean velocity profile for a generalized supersonic shock-free elliptic jet.

4.2 Numerical Analysis

A hybrid numerical scheme is used to solve the stability problem defined by equations 4.3 to 4.7. Hybrid techniques are numerical methods which combine series approximations with finite difference calculations. The present scheme uses a pseudospectral series based on the Chebyshev polynomials to generate the discrete representation of the Rayleigh problem.

In the present study, the pseudospectral series approximates the large scale pressure fluctuation, \hat{p} , in the azimuthal direction, while the finite difference technique approximates \hat{p} in the radial direction. On the edges of the jet cross section, the Rayleigh equation reduces to the Helmholtz equation. This equation has exact analytic solutions in terms of Hankel functions of the first and second kinds. These solutions are used to define the boundary conditions on the edges of the jet.

Moreover, the boundary conditions cutting through the jet, are based on the periodicity of \hat{p} . It may be

shown that either \hat{p} or $\partial\hat{p}/\partial\theta$ is zero on the major and minor axes of the jet cross section. This allows the computational region to be restricted to one quadrant of the shear layer, as shown in figure 13.

Once the boundary conditions cutting through the jet are applied to the pseudospectral series, the exact solutions on the edges of the shear layer are used as initial conditions to integrate the Rayleigh equation. The integrated solutions of the stability problem are then matched at the center of the shear layer using a generalised shooting technique. The matching process generates a matrix of solution vectors which are implicit functions of a fixed real frequency and some guessed complex wavenumber. This implies that the unknown wavenumbers, α_c , may be determined by requiring that the determinant of the solution matrix be zero. The present method applies the iterative Newton-Raphson scheme to compute the wavenumbers.

Details of the hybrid numerical scheme and examples of the stability computations for incompressible non-circular jets are given in ref. 3.

5.0 COMPUTATIONAL RESULTS

In this section the Rayleigh problem governing the linear inviscid isothermal stability of the compressible elliptic jet is solved using the hybrid numerical scheme described in the section 4.3. Calculations are performed to compute the wavenumbers for the jet at the axial stations located at $X = 0.25L_c$ and $X = 0.50L_c$. These calculations are performed for the four azimuthal normal modes corresponding to the varicose, flapping, and the off axis instabilities. The instantaneous pressure for these instabilities is shown in figure 14, ref. 14. In addition, the Strouhal numbers associated with the neutral stability point for the varicose instability are computed for the axial stations between $X = 0.25L_c$ and $X = 0.60L_c$ at increments of $0.05L_c$.

5.1 Stability Analysis

For all the numerical experiments, the aspect ratio of the half velocity point and the equivalent radius, defined by equation 4.5, have been fixed at:

$$\frac{A}{B} = 1.88 \quad (5.1)$$

and

$$L = 1.0 \quad (5.2)$$

respectively. The value of 1.88 for the aspect ratio of the jet was chosen by plotting the aspect ratio of the half velocity point as a function of axial distance, figure 15. This aspect ratio describes an average shear

layer geometry for the jet which includes the effect of the bulge on the minor axis. It should be noted, however, that if the nozzle imperfection were removed the aspect ratio for the jet would increase to a value slightly greater than 2.0.

In addition to fixing the aspect ratio and the reference length scale, the momentum thickness must be determined for the calculations. From figure 12, it is seen that the momentum thickness is nearly constant on the major and minor axes down to the end of the potential core. Therefore, the momentum thickness for the minor axis is taken to be a linear function of axial distance. Then from figure 12, the momentum thickness for the calculations is defined to be

$$\theta_B = 0.112(X/L_c) + 0.004 \quad (5.3)$$

for $0.25 \leq (X/L_c) \leq 0.60$.

The program to solve the Rayleigh problem was verified for incompressible and compressible examples in Baty, ref. 12. For all the jet cross sections considered, the hybrid method was run with 7 interior grid points and a finite difference step size on the order of 0.005. Figure 16 shows the variation of the axial growth rate as a function of frequency for the varicose instability of the jet at $X = 0.25L_c$. The variation of the phase velocity, given by $\omega/Re(\alpha_c)$, is shown in figure 17. These results are typical of all the calculations for the four instabilities of the elliptic jet. To determine the most unstable modes for the different instabilities the three largest growth rates were interpolated using a second order polynomial. Table 1 shows the frequencies of the maximum growth rates for the elliptic jet for several instabilities at the two axial stations of $X = 0.25L_c$ and $X = 0.50L_c$.

L_c	Mode	Freq	Wavenumber
0.25	V	4.00	7.40 - 2.44i
0.50	V	2.24	3.85 - 1.71i
0.25	Fa	3.90	7.30 - 2.65i
0.50	Fa	2.51	4.24 - 1.96i
0.25	Fb	3.86	7.02 - 2.41i
0.25	Of	4.41	7.45 - 1.75i

Table 1: Examples of the maximum growth rates and their associated frequencies for the Mach 1.52 elliptic are shown for the axial stations of $X = 0.25L_c$ and $X = 0.50L_c$. Here, V is the varicose instability; Fa is the flapping instability about the major axis; Fb is the flapping, instability about the minor axis; and Of is the off axis, peanut shaped instability.

In addition to computing the most unstable modes, the neutral frequency as a function of axial length was predicted for the varicose instability. The varicose instability was chosen for the calculation, because the experimental measurements in section 3.2 suggested

that this was the main instability for the shock free elliptic jet. Figure 16 shows the neutral frequency for this instability at the axial station of $X = 0.25L_c$. As discussed in Liou, ref. 16, the neutral frequency at a given jet cross section represents the peak frequency of the large scale structure at that location in the jet. The only peak frequency measured experimentally was the frequency associated with the noise directed to the narrow cone along the jet axis from a region near the end of the potential core. This frequency corresponds to an approximate Strouhal number of 0.19. Results from studies on axisymmetric jets, ref. 9, show that this frequency is close to the large scale instability frequency near the end of the potential core. In figure 18, the predicted neutral frequencies are plotted as Strouhal numbers for axial length nondimensionalized with respect to the potential core length.

5.2 Discussion

Both the experiment and linear inviscid spatial stability theory show that only the lowest order azimuthal modes govern the stability of the supersonic elliptic jet. Experimentally, the varicose mode is found to dominate all other modes, particularly those frequencies that dominate sound radiation from the jet. Seiner, et al., ref. 17, showed that for the round jet the varicose (i.e. axisymmetric) instability dominates all other instabilities for shock free jet plumes. Plumes that contain shocks are often dominated by flapping about a major axis. The elliptic jet results appear consistent with the previous round jet data.

The experimental results in reference 9 and those of Troutt and McLaughlin, ref. 18, indicate that the frequency associated with peak amplitude emission for round shock free supersonic jets is associated with a region near the end of the potential core. In the present experiment, this measured frequency corresponds to a Strouhal number of 0.19. The analysis indicates, that for the varicose instability, this Strouhal number dominates the flow in a region near 60 percent of the potential core. This feature of the linear stability analysis has been observed previously, ref. 9, for round jets, where it is conjectured that large scale waves grow more rapidly in an initially laminar jet column. The spatial stability analysis, which assumes a laminar shear layer with a superimposed large scale fixed frequency wave, has always achieved better agreement to experimental results for lower Reynolds number jets. What effect the simulation of mean velocity profiles has on the spatial stability analysis is unclear, except as noted in reference 9, the analysis is extremely sensitive to second order derivative properties of the assumed mean velocity profile.

The substantial growth in the major axis momen-

tum thickness at the end of the potential core is possibly related to decay of the most amplified wave in the jet column. An unfortunate consequence of the present is that it cannot predict such behavior. There is a strong need to understand the mechanism behind such behavior, since control of the jet's spread rate could possibly be affected through manipulation of the small nonlinearity controlling the major axis momentum thickness.

6.0 CONCLUSIONS

This paper presents the results of linear inviscid spatial stability theory used to calculate the most highly amplified modes of the large scale coherent structures in the supersonic shock free elliptic jet. The results of the analysis have shown that only the lowest order instabilities are significant and that the frequencies for the maximum growth rate decrease with axial distance from the nozzle. In a parallel effort an elliptic nozzle with an exit aspect ratio of 2 was studied to verify the analytical results. This nozzle was designed for an exit Mach number of 1.5. The experimental results indicated that the varicose instability was the dominant spatial mode when operating the nozzle at its shock free point, a result consistent with round jet observations. This result is in agreement with the theoretical analysis in this paper. The measured frequency associated with peak amplitude noise radiation is found to agree reasonably with that frequency predicted to dominate the large scale structure near the end of the potential core.

The present results provide encouragement for use of the inviscid Rayleigh equation to provide a reasonable model to account for dynamical processes associated with non-circular jets. To improve the present quantitative agreement with experiment may require a better description of the real mean flow. In its present form, the determination of a fixed frequency wave's neutral point is computationally intensive. This suggests that more efficient numerical methods are needed to solve the spatial stability problem.

The authors wish to thank Mr. Bernie Jansen for his help in acquiring the aerodynamic data associated with this research. The authors also wish to thank Dr. Glenn Laguna of Sandia National Labs for his help in setting up the batch processes needed to perform the computational experiments.

7.0 REFERENCES

1. Tam, C. K. W., "Stochastic Model Theory of Broadband Shock Associated Noise from Supersonic Jets," *J. Sound Vib.*, 116, 1987, pp 265-302.

2. Morris, P. J., "Instability of Elliptic Jets," *AIAA J.* 26, No. 2, 1988, pp. 172-178.
3. Baty, R. S. and Morris, P. J., "Instability of Jets of Arbitrary Geometry," *AIAA Paper No.* 89-1796.
4. Seiner, J. M., Baty, R. S., and Kumar, A., "A Procedure for the Design of Elliptic Supersonic Shock Free Nozzles," to appear.
5. Pinckney, S. Z., "A Short Static-Pressure Probe Design for Supersonic Flow," *NASA TN D-7978*, 1975.
6. Hubbard, H. H. and Manning, J. C., "Aeroacoustic Research Facilities at NASA Langley Research Center - Description and Operational Characteristics," *NASA TM-84585*, 1983.
7. Yu, J. C. and Dosanjh, D. S., "Noise Field of a Supersonic Mach 1.5 Cold Model Jet," *JASA* 51, No. 5, Part I, May 1972, pp. 1400 - 1410.
8. Tam, C. K. W. and Burton, D. E., "Sound Generation by Instability Waves of Supersonic Flows. Part 2. Axisymmetric Jets," *J. Fluid Mechanics*, 138, 1984, pp. 273-295.
9. Seiner, J. M., McLaughlin, D. K., and Liu, C. H., "Supersonic Jet Noise Generated by Large Scale Instabilities," *NASA TP-2072*, 1982.
10. Ho, C. M. and Gutmark, E., "Vortex Induction and Mass Entrainment in a Small Aspect Ratio Elliptic Jet," *J. Fluid Mech.*, 179, 1987, pp. 383-405.
11. Bridges, J. E. and Hussain, A. K. M. F., "Roles of Initial Condition and Vortex Pairing," *J. Sound Vib.*, 117, Part 2., 1987, pp. 289-311.
12. Baty, R. S., "Reynolds Stress Closure in Jet Flows using Instability Wave Modeling," Ph. D. Thesis, The Pennsylvania State University, 1989.
13. Michalke, A., "Instabilität eines kompressiblen runden Freistrahls unter Berücksichtigung des Einflusses der Strahlgrenschichtdicke," *Z. Flugwiss.*, 19, 1971, pp. 319-328.
14. Morris, P. J. and Miller, D. G., "Wavelike Structures in Elliptic Jets," *AIAA Paper* 84-0399, 1984.
15. Gutmark, E. and Ho, C. M., "Near Field Pressure Fluctuations of an Elliptic Jet," *AIAA Paper No.* 83-0663, 1983.
16. Liou, W. W. W., "Weakly Nonlinear Models for Turbulent Free Shear Flows," Ph. D. Thesis, The Pennsylvania State University, 1990.

17. Seiner, J. M., Manning, J. C., and Ponton, M. K., "The Preferred Spatial Mode of Instability for a Mach 2.0 Jet," AIAA Paper No. 86-1942, 1986.
18. Troutt, T. R. and McLaughlin, D. K., "Experiments on the Flow and Acoustic Properties of a Moderate-Reynolds-Number Supersonic Jet," J. Fluid Mech., **110**, 1982, pp. 123-156.

8.0 FIGURES

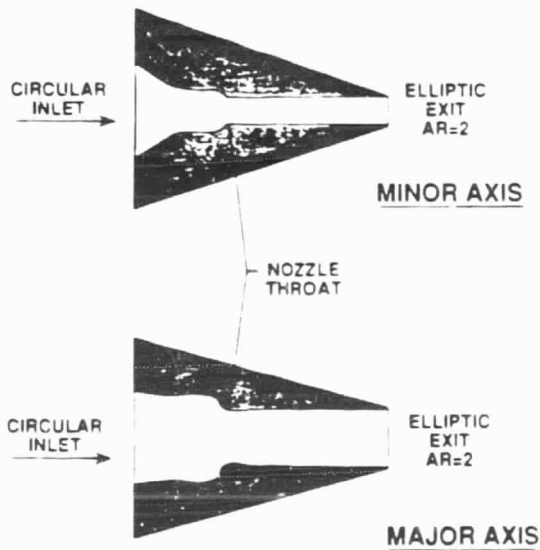


Figure 1: Internal geometry of the elliptic nozzle, major and minor axes cross sections.

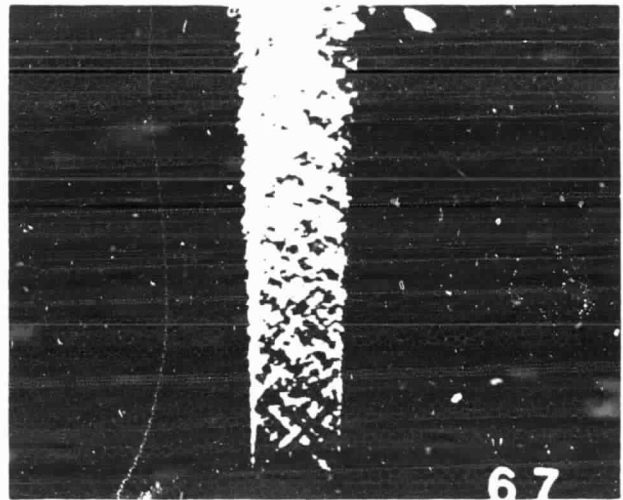


Figure 2a

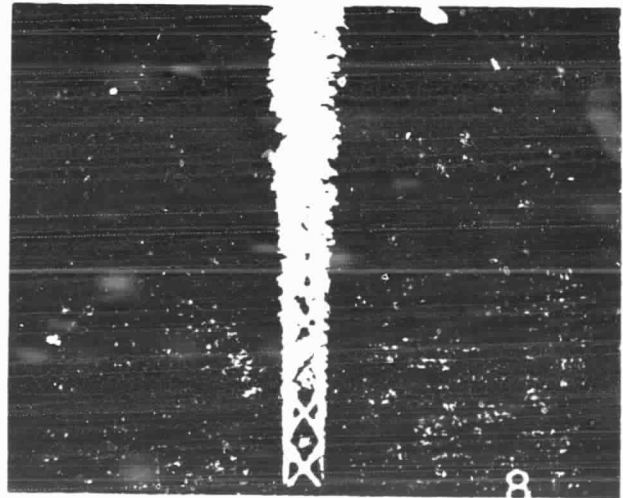


Figure 2b

Figures 2a-b: Schlieren photos showing the major and minor axes of the elliptic jet operating at the design conditions

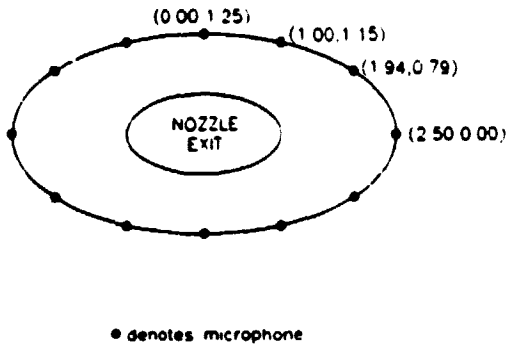


Figure 3: Elliptic near field microphone array.

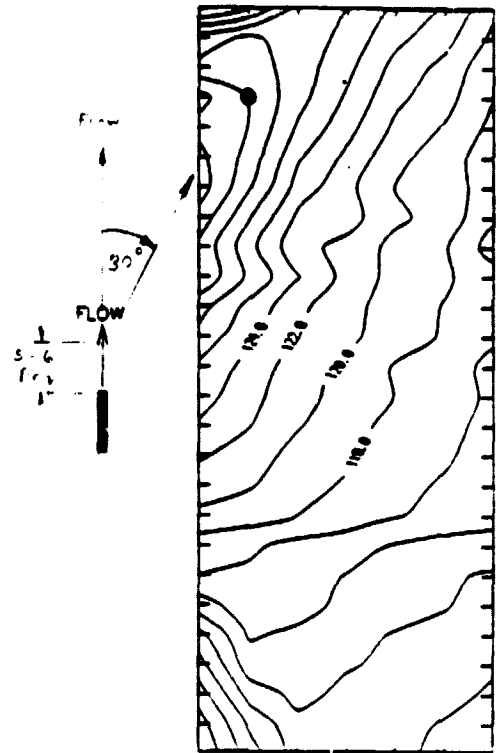


Figure 5: Contour map of OASPL data, $M_d = 1.5$, $M_j = 1.52$.

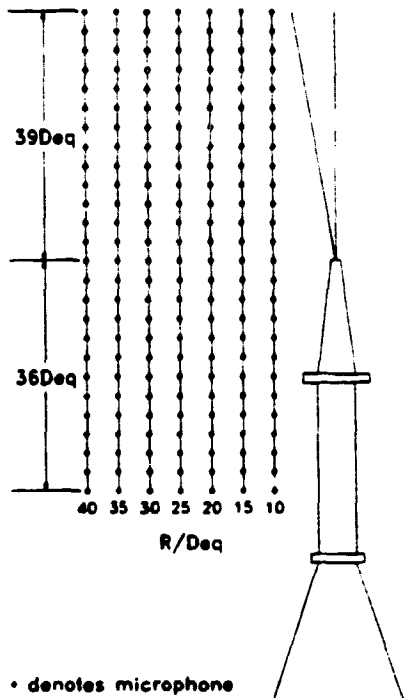


Figure 4: Seven radial positions for the linear microphone array.

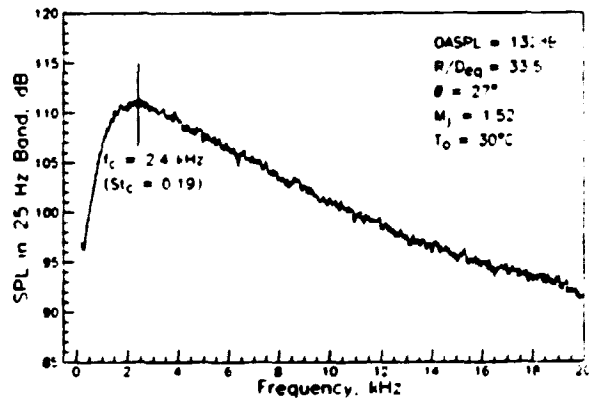


Figure 6: Example narrow band acoustic spectrum in major noise producing region along minor axis.

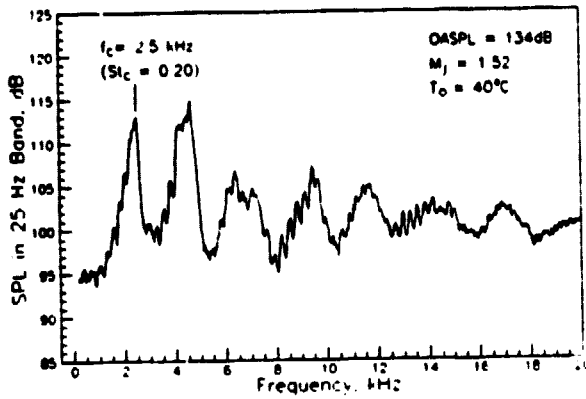


Figure 7: Nossle exit near field pressure spectrum in minor axis plane.

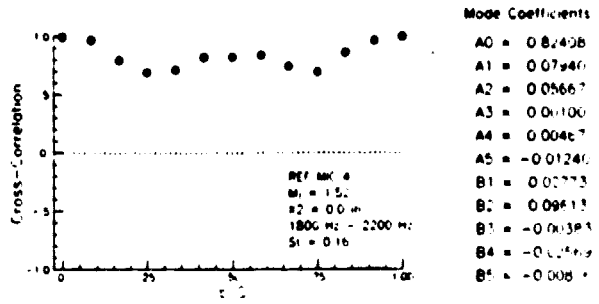


Figure 8c

Figures 8a-c: Asimuthal distribution of 1/3 octave band cross correlation coefficients with modal amplitudes: a. 1000 Hz band, b. 1630 Hz band, and c. 2000 Hz band.

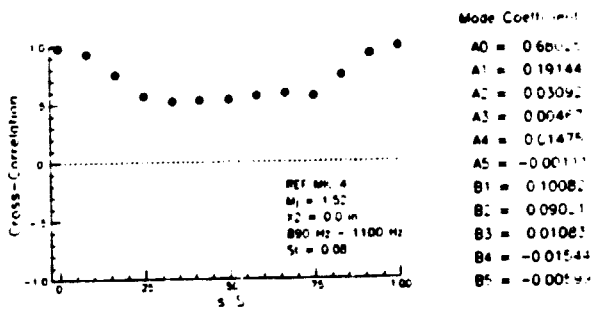


Figure 8a

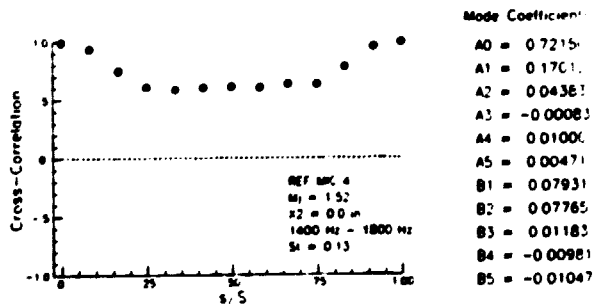


Figure 8b

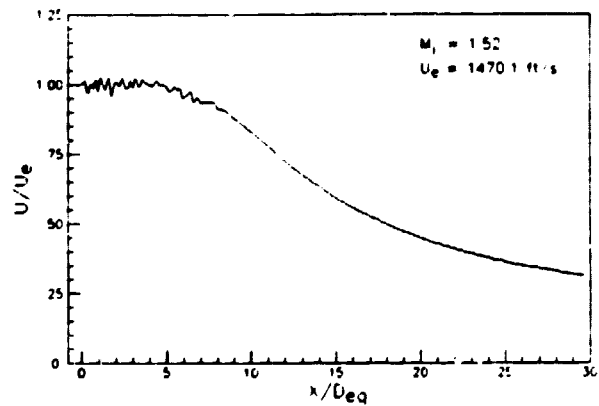


Figure 9: Centerline distribution of mean axial velocity.

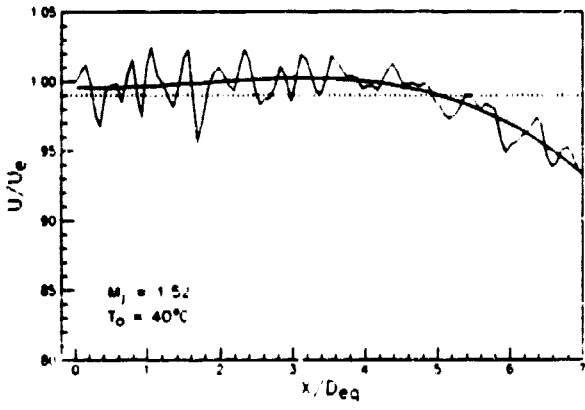


Figure 10: Determination of potential core length.

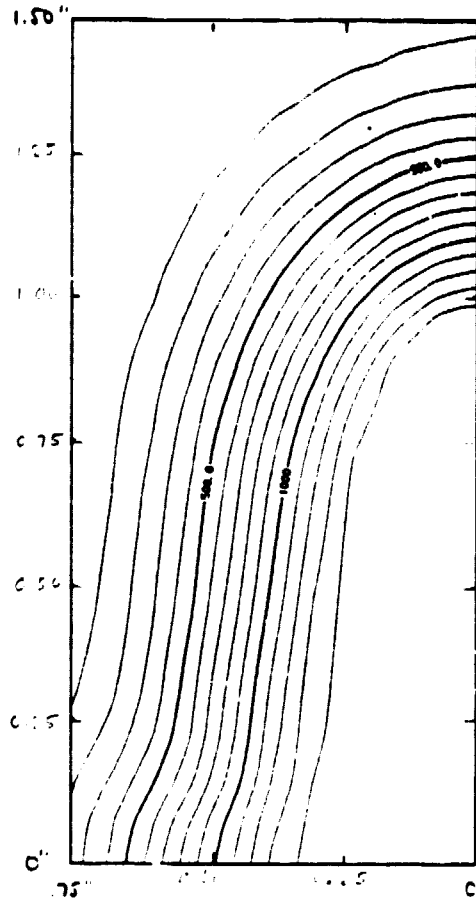


Figure 11b

Figures 11a-b: Contour maps of axial mean velocity: a. $X = 0.25L_c$ and b. $X = 0.50L_c$.

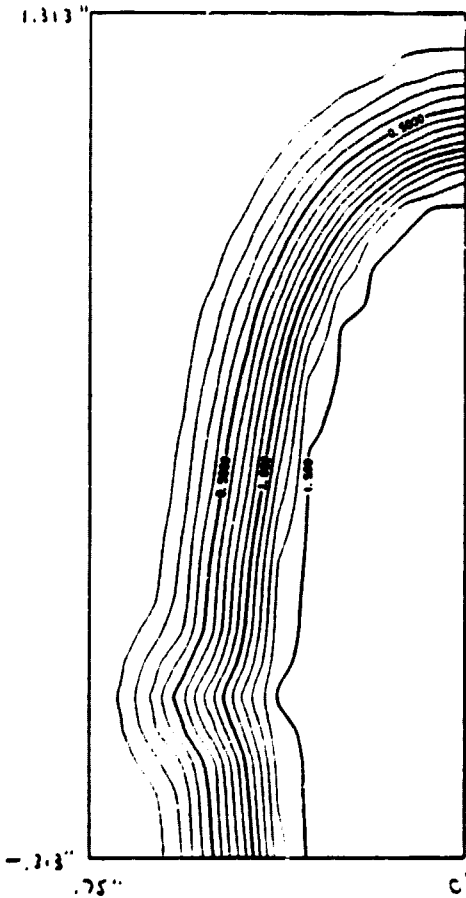


Figure 11a

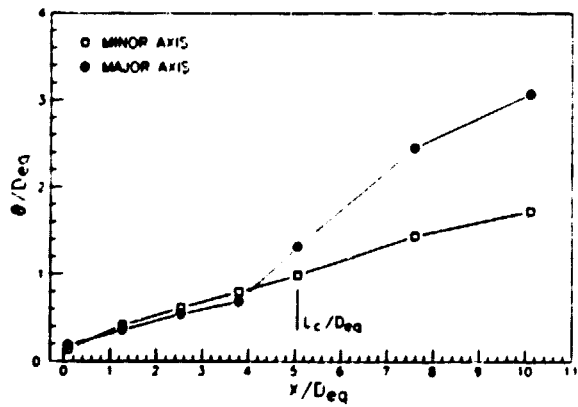


Figure 12: Axial distribution of major and minor momentum thicknesses.

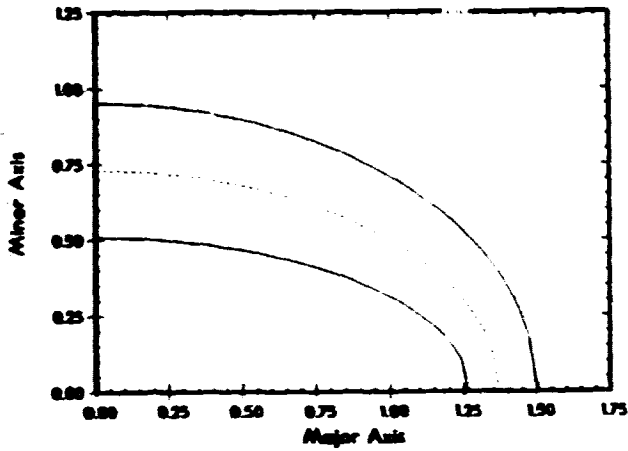


Figure 13: Jet π del cross section at $0.25L_c$ showing constant mean velocity curves in nondimensional coordinates.

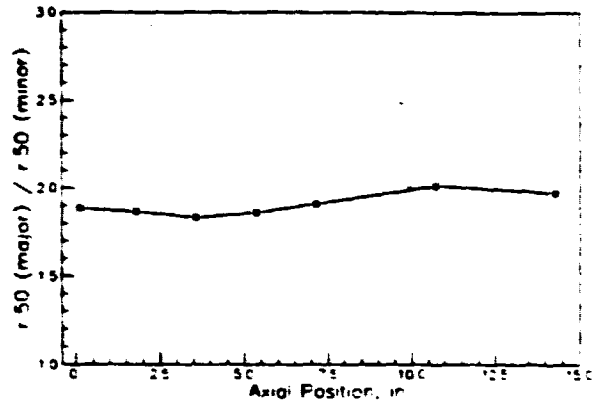
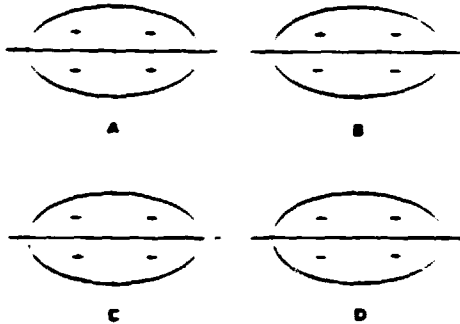


Figure 15: Aspect ratio of the elliptic jet's half velocity point as a function of axial distance.



Figures 14a-d: The azimuthal instantaneous pressure conditions for the four instabilities: a. varicose, b. flapping about the major axis, c. off axis (peanut shaped), and d. flapping about the minor axis.

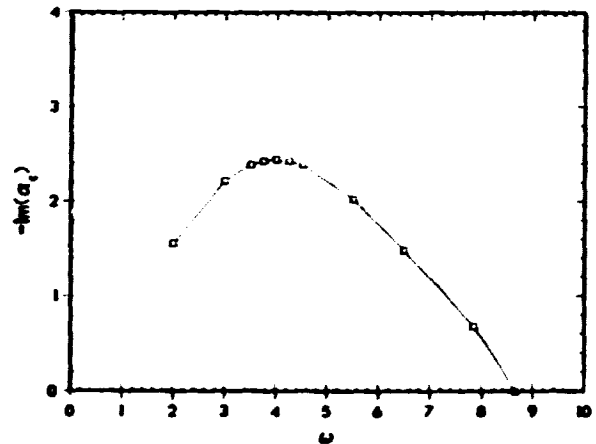


Figure 16: Variation of the axial growth rate with frequency. Varicose instability for the elliptic jet at $X = 0.25L_c$

DISCLAIMER

This report was prepared as an account of work sponsored by an agency of the United States Government. Neither the United States Government nor any agency thereof, nor any of their employees, makes any warranty, express or implied, or assumes any legal liability or responsibility for the accuracy, completeness, or usefulness of any information, apparatus, product, or process disclosed, or represents that its use would not infringe privately owned rights. Reference herein to any specific commercial product, process, or service by trade name, trademark, manufacturer, or otherwise does not necessarily constitute or imply its endorsement, recommendation, or favoring by the United States Government or any agency thereof. The views and opinions of authors expressed herein do not necessarily state or reflect those of the United States Government or any agency thereof.

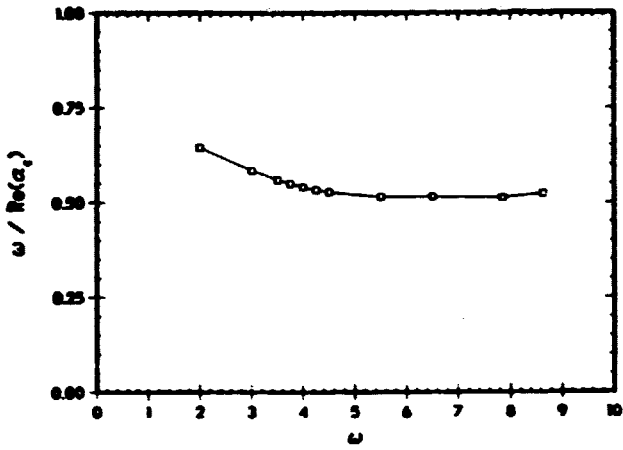


Figure 17: Variation of the phase velocity with frequency. Varicose instability for the elliptic jet at $X = 0.25L_c$.

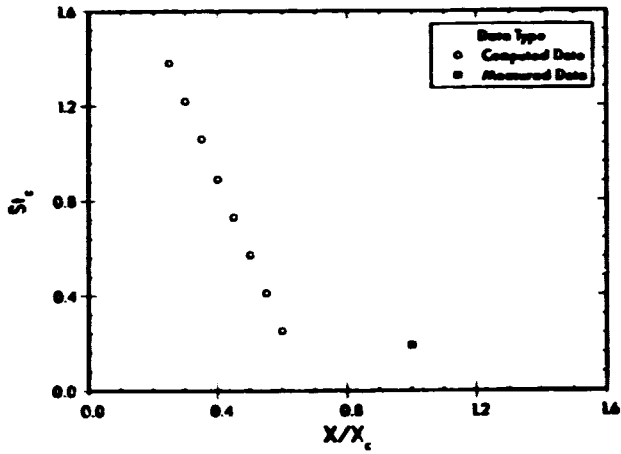


Figure 18: Variation of the neutral Strouhal number with axial length for the varicose instability